COMBINED OPTICAL AND RADAR MEASUREMENTS FOR ORBIT DETERMINATION IN LEO

R. Apa[1], S. Bonaccorsi[1], L. Pirovano[2], and R. Armellin[3]

[1]*Institut Supérieur de l'Aéronautique et de l'Espace (ISAE-SUPAERO), Université de Toulouse, 31055 Toulouse, FRANCE, Email: {riccardo.apa, sergio.bonaccorsi}@student.isae-supaero.fr*
[2]*Surrey Space Centre, University of Surrey, Guildford GU2 7XH, UK, Email: laura.pirovano@auckland.ac.nz*
[3]*Institut Supérieur de l'Aéronautique et de l'Espace (ISAE-SUPAERO), Université de Toulouse, 31055 Toulouse, FRANCE, Email: r.armellin@isae-supaero.fr*

ABSTRACT

In the context of Space Surveillance and Tracking, one of the crucial phases of the cataloguing process is the identification of newly detected objects and their initial orbit determination (IOD). We propose an analysis of the combined use of radar and optical instruments in a stare and chase strategy as follows. Through a large field of view staring optical camera, the prediction of new SOs' trajectory is obtained. This is then sent to a radar instrument which performs the chasing phase. The radar pointing law is obtained either through a quadratic regression of the optical observations or through the propagation of an optical IOD solution, depending on the quality of the optical measurements. This approach aims to merge the precise optical angular measures with the precise radar range measurements to achieve better IOD solutions. An optimization criterion based on the maximisation of the number of detected objects and the accuracy of the determined orbits was used to optimally point the optical camera, for each place at any time of the year. At the end of the operations, very accurate results in terms of orbit determination were found, proving that this strategy may represent a valid alternative in the future.

Keywords: Space Situational Awareness; Space Surveillance and Tracking; Orbit determination; Stare and Chase.

1. INTRODUCTION

The exploitation of space over the last fifty years has led to an increase in the population of debris orbiting around the Earth. To improve Space Surveillance, and thus avoid dangerous collisions, this great amount of space objects must be classified. In particular, we focus on Low Earth Orbit (LEO) unknown debris (from 0.2 m to 1.2 m of diameter) because of the great number of active satellites present in this region. LEO tracking is generally operated by military radars which present different problems such as high costs, private facilities and scarce precision in initial orbit determination (IOD) due to raw angular measures. Optical sensors are mainly used to monitor geostationary (GEO) orbits because GEO is too remote for radar observation [1]. Using these instruments for the LEO region is not an easy task due to its dependence on lighting and weather conditions. For these reasons their capabilities related to the observation time have been examined and tested in different recent studies [2]. Today, surveillance sensors, devoted to characterisation of the near-Earth environment, use fixed or predefined pointing laws leading to short observation arcs and poor orbital information. *Stare and chase* is a strategy which allow to overcome this limit thanks to the combination of two sensors working in two different modes [3]. Sensors in stare mode detect all objects passing through their FoVs, while sensors in chase mode are ready for an immediate tracking of the detected objects. Stare observations are processed as soon as they are collected to obtain trajectory predictions of the object for the tracking sensors as fast as possible. We want to investigate the potential of this strategy using a large FoV optical camera as the staring sensor and existing radar observatories as the chasing sensors.

The aim of this research is to study the potential of the combined use of optical and radar instruments for cataloguing purposes. This strategy can combine the low-cost and more practical optical cameras together with existing radar observatories in order to increase the number of detected space objects and get more accurate orbital knowledge. The latter can be achieved by combining high-precision optical angular measures with those of high-precision radar range. The interest in such research is therefore justified by the possibility of reducing the costs associated with this activity through the implementation of an easily realizable system. To achieve our main purpose we focused on some related objectives. We investigated the information we can extract from observations that relied on polynomial regression or the Gauss method in order to study the possibility of deriving a chasing law. We analysed the uncertainties related to the previous operations to determine the maximum time allowed for radar acquisition and the need for co-location of the ob-

servatories. In addition, we created an algorithm to find the optimal pointing of the large FoV optical camera. All these objectives were studied according to two different system implementation strategies. The first deals with the use of an observatory with both instruments; the second with two separate observatories using only the optical or radar instrument. The paper is structured as follows: in Section 2 we describe schematically the whole adopted procedure and the two strategies we studied. In Section 3 we recall the main mathematical tools we made use of. In Section 4 we report the methods we developed specifically for solving the problem. In Section 5, we report some results and test cases. Finally, in Section 6 we discuss what we propose to improve and what we will deal with in future works.

2. OVERVIEW

We can better describe the steps of the procedure thanks to the diagram in Fig. 1, whose blocks will be detailed later. It represents the flow of operations starting from the acquisition of optical measurements of an uncatalogued space object until the related orbit determination (OD) (if possible). Simulations of optical observations are obtained by using a tool called Virtual Observatory (VO), detailed in Section 3.1. The first step is the convergence analysis of the Gauss method using the newly obtained data, performed according to [9] and better explained in Section 3.2. The strategies we studied share a branch of operations. In the case of separate optical and radar observatories, an IOD must be available to allow the calculation of the chasing law defined with respect to another point on the Earth's surface. For this reason, the green dotted block in the diagram contains only the operations that follow the convergence of the Gauss method, which is detailed in Section 3.3. In case of non-convergence, the strategy with the two instruments in the same position can continue extrapolating a predicted trajectory through polynomial regression (PR) of the set of observations, as explained in Section 3.4. For both branches, radar measurements are taken only if the detection probability (DP) test gives positive answer, otherwise the flow is interrupted. DP is described in Section 4.1.
In case of failure of the DP test or the recapturing phase, the two branches lead to different results. In the right branch, where an angles-only IOD has not been calculated, we only have a set of observations and their regression coefficients, so we are not able to perform any kind of OD and we consider the procedure a failure. In the left branch, we already have an IOD, so the procedure can be considered a success even if the precision of the results has not been refined through a least-squares (LS) procedure involving radar measurements. This procedure will be described in Section 3.5. In case radar measurements are taken, we are able to achieve an accurate orbital knowledge through the combined use of two high-precision measurements. The two strategies mentioned above are detailed in the next sections.

2.1. Co-located optical and radar observatories

This strategy consists in keeping the optical camera in the same location as the radar observatory, thus resulting in time reduction in calculating and sending the chasing law to the steerable radar. The advantages of this case are that the two instruments have the same pointing at the beginning (so the radar is quite fast in pointing the predicted trajectory) and that the polynomial regression is also applicable when the IOD with the Gauss method fails. The disadvantage is that the two instruments work best in different scenarios so the optical sensors could be penalized by the lower altitude location typical of radar observatories.

2.2. Separate optical and radar observatories

Optical sensors need very specific location to overcome visibility constraints, as already stated. For this reason, the first strategy could limit the number of objects detected by optical cameras, and the second strategy aims to break through this dependence by positioning the optical instrumentation in a more adapted place, different from radar observatory. The disadvantage is that we are dealing with two different positions on the Earth's surface, so the extrapolation of the chasing law for radar has to be derived through inertial coordinates. In addition, the time for data handling is affected as described in Section 5.3.

3. TOOLS

This work is based on the use of optical and radar observations. For this reason a fundamental tool is the so-called Virtual Observatory, which is able to create synthetic measurements. Other mathematical tools, already mentioned in 2, were used on the results of such simulations to create new methods. These methods were then applied to find a solution to the objectives proposed in the introduction.

3.1. Virtual Observatory (VO)

A fundamental part of this work involved the creation of synthetic measurements to test and validate algorithms and study their sensitivity to different observation schedules. For this reason a Virtual Observatory was used. This software is able to recreate optical and radar survey scenarios from any point on Earth, thanks to the use of Spacecraft Planet Instrument C-matrix Events (SPICE), a powerful tool developed by the Navigation and Ancillary Information Facility (NAIF) group at NASA [4]. In order to create simulations, two-line elements (TLEs) of the space object of interest are fed into the software. These files contain data that represent the ephemerides of the objects for a certain time interval. Thanks to this

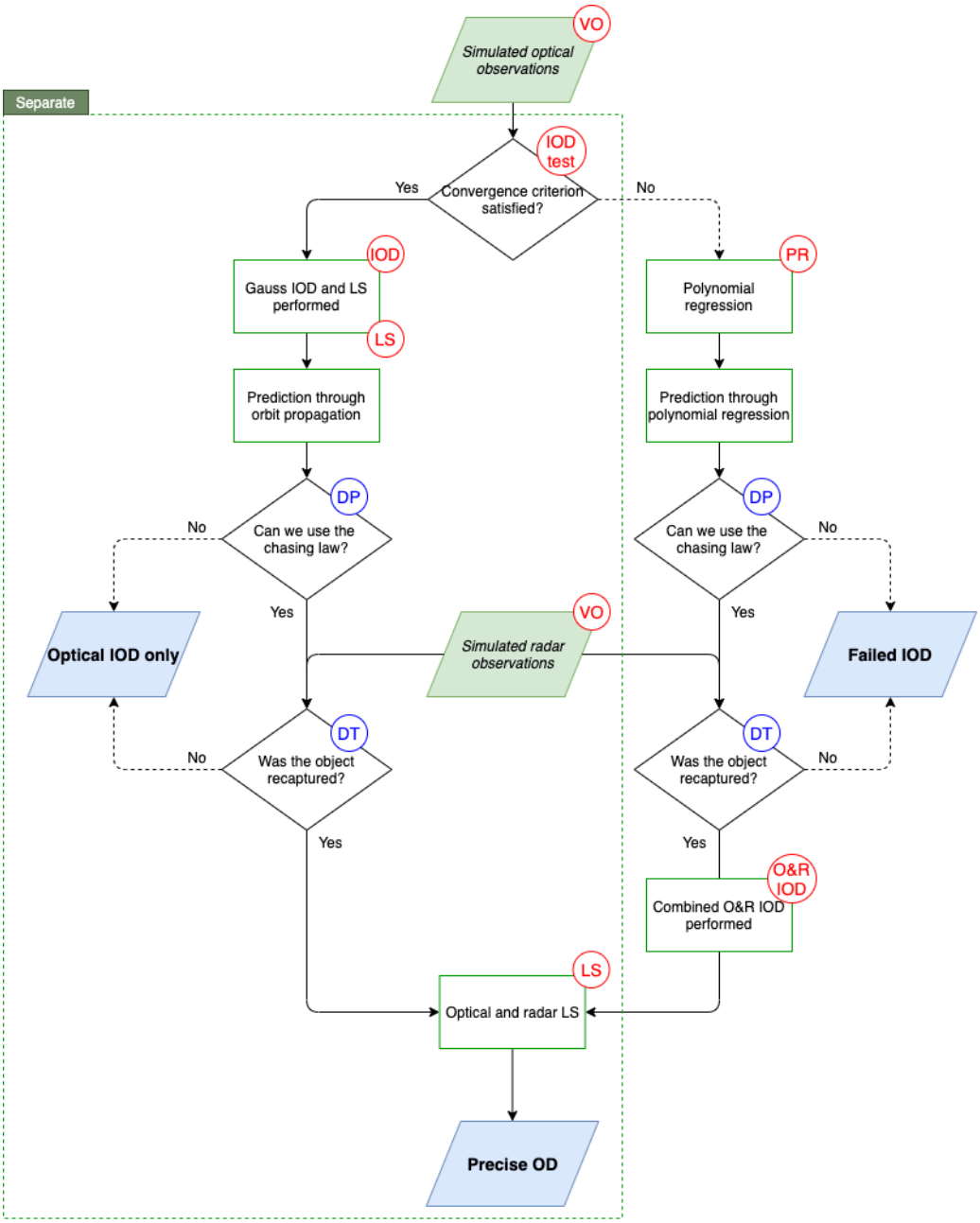

Figure 1. Flow diagram

information, the states of the object and the desired observatory are created. The relative geometry analysis and the application of different constraints enable the definition of the so-called tracklets, which are sequences of N observations collected in a certain amount of time. The constraints used in the simulation are related to sky background luminosity, object illumination, object elevation, object relative position with respect to Sun and Moon. Lastly, the observations are simulated by defining the sensor type and by adding user-defined measurement noises. More details about the VO are given in [5].

3.2. Convergence analysis for Gauss's method (IOD test)

The best possible case is to obtain an IOD immediately after the optical measures have been taken, so that a more precise chasing law can be defined. Unfortunately, we cannot be sure that the Gauss method will converge by using the data of each optical tracklet. For this reason, once the optical measurements are available, an analysis is performed in order to check if the Gauss method will converge using these data. For this aim, the Signal to Noise Ratio (SNR) of the line-of-sight matrix determinant is estimated through the procedure described in

[9]. Given a set of three angle-pair measurements and the associated measurement uncertainty, this quantity can be used to estimate whether the point-valued solution produced by Gauss's method belongs to a convergent distribution or not. We used this procedure iteratively based on the fact that for LEO objects the presence of a divergent "pinch point" is possible, and even low-noise measurements are expected to produce a divergent solution space. Initially, the first, the middle, and the last angle-pair measurements of the tracklet are selected. Then, if the threshold criterion for convergence is not satisfied, we take a reduced version of the same tracklet (we cut the last elements), and we take again the first, the middle, and the last angle-pair measurements, so that the time shift between the three pieces of data is also reduced. If a good set of three angle-pair measurements is found, then an IOD is obtained through Gauss's method.

3.3. Gauss's Method (IOD)

The Gauss method of angles-only orbit determination takes as input three times of observations (t_1, t_2, t_3), the observatory's positions for those times $(\mathbf{R_1}, \mathbf{R_2}, \mathbf{R_3})$ and the direction cosine vectors $(\hat{\boldsymbol{\rho}}_\mathbf{1}, \hat{\boldsymbol{\rho}}_\mathbf{2}, \hat{\boldsymbol{\rho}}_\mathbf{3})$. The algorithm estimates the slant ranges (ρ_1, ρ_2, ρ_3) in order to obtain the object positions for $i = 1, 2, 3$

$$\mathbf{r_i} = \mathbf{R_i} + \rho_i \hat{\boldsymbol{\rho}}_\mathbf{i} \tag{1}$$

in two-body dynamics. Detailed description of the algorithm can be found in [6]. In our work Gauss's method has been used for those sets of optical observations that allow good results in terms of convergence according to the analysis previously described, in order to get an IOD that is then used to extract the chasing law needed for the radar observation phase.

3.4. Polynomial Regression (PR)

Polynomial regression is a mathematical process that models the relation between two variables through an n-th degree polynomial. In order to construct the curve that best fits a series of data points, the method of least-squares, which minimizes the sum of the squares of the residuals, is typically used.
For our purposes polynomial regression was used for both optical and radar observations, which are defined in the time spans

$$\left[t_0^O; t_f^O\right] \quad \text{and} \quad \left[t_0^R; t_f^R\right]$$

In the case of optical observations, this procedure was used to derive an estimate for the short-term trajectory of the space object. This information is then extrapolated in time in order to get a predicted trajectory used as a chasing law for radar observation phase. Concerning radar range measurements, they are also fitted through a second order polynomial in order to allow the calculations performed by the IOD method described in Section 4.3. The series of data points to be fitted are the observations contained in the optical tracklets. They usually contain three or more observations, each observation being made of a right ascension (RA) α, a declination (Dec) δ, a precision σ and a time of observation t. Time is thus used as an independent variable and two different curves are obtained for α and δ. In our work the most used curve is the quadratic polynomial.

$$\alpha(t) = a_0 t^2 + a_1 t + a_2 \tag{2}$$

$$\delta(t) = d_0 t^2 + d_1 t + d_2 \tag{3}$$

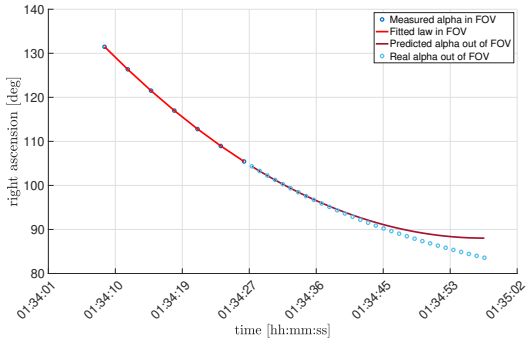

Figure 2. Example of regression on right ascension

Regression can be conveniently performed at the central time of optical observations such that smaller uncertainties on the observed angles are obtained at the beginning and the end of the confidence region. This kind of approach is thus convenient for the IOD calculations of the Gauss method.

3.5. Non linear weighted least-squares (LS)

Given a set of N measurements affected by errors and a parametric function, the least-squares method aims to determine those parameters which minimize an objective function J. Let $f(t, \boldsymbol{x})$ be a parametric function with t as independent variable and $\boldsymbol{x}$ as the M-dimensional parameters vector. If (t_i, y_i) represents the i-th measurements of a physical event associated with the weight w_i, the least-squares criterion foresees the minimization of the so-called residual equation

$$J = \sum_{i=1}^{N} w_i^2 \bar{r}_i^2 = \bar{\boldsymbol{r}}^{\boldsymbol{T}} \boldsymbol{W} \bar{\boldsymbol{r}} \tag{4}$$

where

$$\bar{r}_i = y_i - f(t_i, \boldsymbol{x}) \tag{5}$$

is only dependent on the unknown parameters, and the weighting matrix is

$$\boldsymbol{W} = diag(\bar{\boldsymbol{w}}) \tag{6}$$

where

$$\bar{\boldsymbol{w}} = \left[\; w_1^2, \ldots, w_N^2 \; \right] \tag{7}$$

We want to find a minimum for J, so the problem to solve is

$$\frac{dJ}{d\boldsymbol{x}} = 0 \tag{8}$$

In practice we used the MATLAB function *lsqnonlin* to find the solution of equation (8). Only an initial estimation of $\boldsymbol{x}$, the so-called guess state $\boldsymbol{x}^0$, is necessary to create an iterative process which, under convergence conditions, provides the solution. For further information, see [7]. In our research, this method was used to refine the IODs by using the whole set of optical measurements, with $\boldsymbol{x}$ the six-component state vector $[r_x, r_y, r_z, v_x, v_y, v_z]$, and y_i the right ascension (α), declination (δ) or range (ρ) measurement affected by errors at time t_i. The guess state $\boldsymbol{x}^0$ is represented by the six-component vector obtained by the Gauss method or the O&R IOD (Sections 3.3 and 4.3). This initial state is then propagated under Keplerian assumptions at the same time as the optical and radar measurements. In order to be used in the iterative procedure, state vectors thus obtained have to be converted into local coordinates α, δ and ρ. Therefore, in our specific case, f is the composition of the orbit propagation function and the conversion function into local coordinates. Concerning the matrix $\boldsymbol{W}$, we considered two different weights linked to the optical and radar instrumentation. Let σ_o be the standard deviation of optical measurements and σ_r the standard deviation of radar measurements, we can explicit the weights matrix components as $w_i = \frac{1}{\sigma_o}$ if $\bar{r}_i$ derives from α or δ measurements and $w_i = \frac{1}{\sigma_r}$ from ρ ones. The iterative process returns the least-squares refined state vector, which can easily be converted into Keplerian elements. Another important output of the function *lsqnonlin* is the Jacobian matrix $\boldsymbol{A}$ which, for Gauss-Newton or Levenberg-Marquardt assumptions, can be used to estimate the Hessian matrix in order to calculate an approximate covariance matrix given by

$$\boldsymbol{C} = \left(\boldsymbol{A^T W A}\right)^{-1} MSE \tag{9}$$

where

$$MSE = \frac{\sum_{i=1}^{N} \bar{r}_i^2}{N - M} \tag{10}$$

This multiplicative term is used to reduce the errors generated by Hessian estimation, which is non-negligible if the residuals are large (see [8] for more details). The covariance matrix is used for error propagation analysis as well as for calculating the state transition matrix, which proved useful for estimating detection probability (see Section 4.1).

4. METHODS

4.1. Estimation of detection probability (DP)

This section explains how we provide a random character to the simulation by using a quantity called *detection probability*. The first step required to calculate this quantity is to perform the uncertainty analysis on the predicted trajectory. As stated before, the latter can be obtained through an IOD or a polynomial regression, depending on the quality of the optical measurements. In both cases, the quantities we need are the uncertainties expressed in azimuth and elevation defined at the start time of radar measurements t_0^R.
In the case of polynomial regression, we can get the Root Mean Square Error (RMSE), which measures the gap between the estimator and the data collected. We define the fitted laws in right ascension and declination from the initial time of optical observation t_0^O until t_0^R, and then we perform the conversion in azimuth and elevation. Finally, we calculate the quantities of interest as follows

$$RMSE_{A,h} = \sqrt{\frac{1}{N} \sum_{i=1}^{N} \bar{r}_{A,h_i}^2} \tag{11}$$

where N is the number of observations and $\bar{r}_i$ is the residual in azimuth or elevation defined as the difference between the simulated and the estimated quantities.
In the case of IOD, we can perform a least-squares refinement by using only optical measurements, and then obtain the corresponding covariance matrix $\boldsymbol{C}$ as described in 3.5. The state vector refined by the least-squares procedure is defined at the central time of optical observations t_c, therefore the covariance matrix must be calculated at a later time to define the uncertainty at the time of interest t_0^R. This procedure is performed by using the state transition matrix of the Keplerian dynamics defined as

$$\boldsymbol{\Phi}(t, t_0) = \boldsymbol{I} + \boldsymbol{A}(t - t_0) \tag{12}$$

where

$$\boldsymbol{A} = \begin{bmatrix} \boldsymbol{0} & \boldsymbol{I} \\ \boldsymbol{G(r)} & \boldsymbol{0} \end{bmatrix}$$

with

$$\boldsymbol{G(r)} = \frac{\mu}{r^5}(3\boldsymbol{r}\boldsymbol{r^T} - r^2\boldsymbol{I})$$

In our case, $\boldsymbol{C}$ is defined in Cartesian state, therefore linear mapping is also necessary to get the covariance matrix in azimuth and elevation. Let $y = f(x)$ be the function that defines the transformation from Cartesian state into

azimuth and elevation, the map $\boldsymbol{M}$ to transform the covariance is defined through finite differences.

$$\boldsymbol{M} = \frac{\partial f}{\partial \boldsymbol{x}} \tag{13}$$

where

$$\frac{\partial f}{\partial \boldsymbol{x}} \approx \frac{f(\boldsymbol{x} + \delta\boldsymbol{x}) - f(\boldsymbol{x} - \delta\boldsymbol{x})}{2\delta\boldsymbol{x}}$$

This procedure requires generating two samples for each state vector element and therefore a total of twelve samples. The steps for defining the uncertainties in azimuth and elevation at t_0^R, can thus be performed as follows:

$$\boldsymbol{C}(\boldsymbol{x}; t_0^R) = \boldsymbol{\Phi}(t_0^R, t_c)\boldsymbol{C}(\boldsymbol{x}; t_c)\boldsymbol{\Phi}^{\boldsymbol{T}}(t_0^R, t_c) \tag{14}$$

$$\boldsymbol{C}(A, h; t_0^R) = \boldsymbol{M}\boldsymbol{C}(\boldsymbol{x}; t_0^R)\boldsymbol{M}^{\boldsymbol{T}} \tag{15}$$

Finally, we obtain the two-by-two matrix from which we can extract σ_A and σ_h, that are the standard deviations in azimuth and elevation.
Once we have the uncertainties in azimuth and elevation, we can compare them with the width of the radar's FoV (FoV^R) in order to get *DP* for both laws. To get these numbers, we integrate a Gaussian distribution with zero mean and variance equal to σ_A^2 or σ_h^2 in the interval

$$\left[-\frac{FoV^R}{2}; +\frac{FoV^R}{2}\right]$$

Once *DP* is available, we compare it with a random number uniformly distributed between zero and one. If the number is below *DP*, the procedure for taking radar measurements begins, otherwise it is considered a failure a priori. In most cases, these numbers were found to be very close to one, thereby highlighting the high accuracy of the chasing laws.

4.2. Delay time for radar measurements (DT)

Both strategies plan to take radar measurements after having approximated the $\alpha(t)$ and $\delta(t)$ time laws of the object from optical measurements. These laws can be useful for pointing small radar FoV in order to take range and range rate measurements. The time delay between the end of optical measurements and the radar capture of the object is taken into account in order to make the simulation more realistic. We can split this delay time into two different parts $t_D = t_{IPF} + t_{RC}$, with t_{IPF} as the time for optical images processing and fitting and t_{RC} as the time needed by the radar to point in the predicted trajectory. In our work the t_{IPF} has been estimated according to [2], while the t_{RC} has been modelled according to the following procedure. The $\alpha(t)$ and $\delta(t)$ predicted laws are firstly converted into azimuth $A(t)$ and elevation $h(t)$ and, once they are fed into the radar, they represent the target positions for the center of the radar's FoV. We notice that t_{IPF} is also the time at which the radar starts moving, so with $A_R(t_{IPF})$ and $h_R(t_{IPF})$ the initial radar positions in azimuth and elevation (which are the same as that of the center of the optical FoV in the case of the co-located strategy), the initial errors are

$$\delta A(t_{IPF}) = A(t_{IPF}) - A_R(t_{IPF})$$
$$\delta h(t_{IPF}) = h(t_{IPF}) - h_R(t_{IPF})$$

In addition, if we suppose that the radar moves with constant slew rate both in azimuth and elevation, respectively $\dot{A}_R$ and $\dot{h}_R$, then the $A_R(t)$ and $h_R(t)$ positions laws of the radar at time t can be obtained as

$$A_R(t) = A_R(t_{IPF}) \pm \dot{A}_R(t - t_{IPF})$$
$$h_R(t) = h_R(t_{IPF}) \pm \dot{h}_R(t - t_{IPF})$$

Intuitively the azimuth and the elevation will increase if the object moves from left to right or upwards the FoV, but will decrease in the opposite case. The time required to chase the object (t_{RC}) is equal to the time required to nullify the errors in azimuth and elevation

$$\delta A(t_{RC}) = A(t_{RC}) - A_R(t_{IPF}) \mp \dot{A}_R(t_{RC} - t_{IPF}) = 0 \tag{16}$$
$$\delta h(t_{RC}) = h(t_{RC}) - h_R(t_{IPF}) \mp \dot{h}_R(t_{RC} - t_{IPF}) = 0 \tag{17}$$

These equations can be solved without any particular difficulty and will return two different values. Given t_{RC_1} and t_{RC_2} these values, we will consider the chasing time as the time at which both (16) and (17) are accomplished

$$t_{RC} = max(t_{RC_1}, t_{RC_2}) \tag{18}$$

The contour plot in Fig. 3 shows the influence of both the t_{IPF}, $\dot{A}_R$ and $\dot{h}_R$, considered as equal and constant, on the t_D. We can remark how t_D is mainly influenced by t_{IPF} because of the slow changes of the object's azimuth and elevation with respect to radar motion laws.

The estimation of the end time for radar measurements t_{RE} can be simply calculated as the minimum time at which the difference between the predicted laws $A(t)$ and $h(t)$ and the real azimuth and elevation of the objects, respectively $A_{real}(t)$ and $h_{real}(t)$, is superior to the mid-amplitude of the FoV of the radar. In equation:

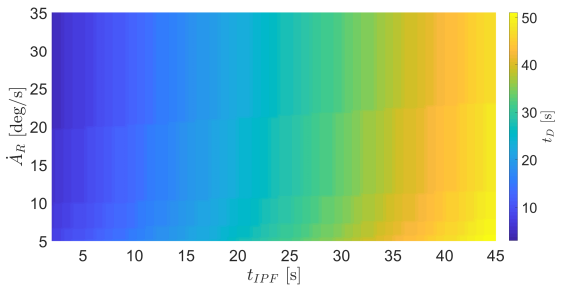

Figure 3. Time needed to recapture the object

$$t_{RE} = min(t_1, t_2)$$
$$t_1 = t : |A(t) - A_{real}(t)| > \frac{FoV^R}{2}$$
$$t_2 = t : |h(t) - h_{real}(t)| > \frac{FoV^R}{2}$$

4.3. IOD from optical and radar measurements (O&R IOD)

If an IOD cannot be acquired through optical measurements due to the lack of convergence of the Gauss method, the polynomial regression strategy is still available. Through the propagation of the fitted laws $\alpha(t)$ and $\delta(t)$, the chasing law is determined and fed into the radar instrument to take the slant ranges. Once a set of range measurements are available, they are used to perform a second order polynomial regression to get the fitted law

$$\rho(t) = r_0 t^2 + r_1 t + r_2 \tag{19}$$

Six independent parameters, defined at the same time instant, are necessary to perform their conversion into position and velocity. The central time of optical observations t_c is used for reference. The values of $\alpha(t_c)$ and $\delta(t_c)$ are taken from their fitted laws so that the presence of noise on the single value can be, somehow, reduced. Concerning range, the regression coefficients r_i $(i = 0, 1, 2)$ of the fitted law $\rho(t)$ are obtained using radar observations, which are defined in the time span that starts from t_0^R. The law $\rho(t)$ allows us to have approximated range values in the whole optical observations time span and in particular at the time t_c. Then, the angles rate and range rate quantities $\dot{\alpha}$, $\dot{\delta}$ and $\dot{\rho}$ are calculated using their respective regression coefficients.

$$\dot{\alpha}(t_c) = 2a_0 t_c + a_1 \tag{20}$$

$$\dot{\delta}(t_c) = 2d_0 t_c + d_1 \tag{21}$$

$$\dot{\rho}(t_c) = 2r_0 t_c + r_1 \tag{22}$$

Once all parameters are collected, they can be converted into the state vector of position and velocity. Since such observations are made from a ground station, the position of the object with respect to the planet center is given as the sum of the position of the ground station and the position of the object with respect to the station, and likewise for the velocities:

$$\mathbf{r}_{\text{obj}} = \mathbf{r}_{\text{obs}} + \mathbf{r}_{\text{obj/obs}} \quad \text{and} \quad \mathbf{v}_{\text{obj}} = \mathbf{v}_{\text{obs}} + \mathbf{v}_{\text{obj/obs}}$$

where $\mathbf{r}_{\text{obj/obs}}$ and $\mathbf{v}_{\text{obj/obs}}$ are given using spherical coordinates.

$$\mathbf{r}_{\text{obj/obs}} = \rho \mathbf{u}_\rho \quad \text{and} \quad \mathbf{v}_{\text{obj/obs}} = \dot{\rho}\mathbf{u}_\rho + \rho\dot{\alpha}\mathbf{u}_\alpha + \rho\dot{\delta}\mathbf{u}_\delta$$

and the vectors $\mathbf{u}_\rho$, $\mathbf{u}_\alpha$ and $\mathbf{u}_\delta$ are given by:

$$\mathbf{u}_\rho = \begin{bmatrix} \cos\alpha\cos\delta \\ \sin\alpha\cos\delta \\ \sin\delta \end{bmatrix}$$

$$\mathbf{u}_\alpha = \begin{bmatrix} -\sin\alpha\cos\delta \\ \cos\alpha\cos\delta \\ 0 \end{bmatrix}$$

$$\mathbf{u}_\delta = \begin{bmatrix} -\cos\alpha\sin\delta \\ -\sin\alpha\sin\delta \\ \cos\delta \end{bmatrix}$$

The state vector obtained through this procedure is then used as a first guess for a least-squares refinement by drawing on all the measurements available from both optical and radar instruments.

4.4. Optimization algorithm for a large FoV optical camera

The FoV of the optical camera is fixed in space, waiting for new objects to pass by. Orbital elements of the population of LEO satellites have an interesting distribution that we want to exploit in order to maximize both the number of detected objects and their probability of being captured by the radar observatory. In practice, we analysed the distribution of LEO satellites according to some orbital parameters of interest, and we extracted a significant number of samples in order to make our simulation statistically relevant, as we will explain later (Section 5.1). We created an algorithm based on simulated LEO tracklets from different observatories, in different time periods over a year, in order to assign a score to each possible optical FoV. This score must take into account the two following main objectives: the number of detected tracklets and mainly their potential to generate a high-precision IOD. To do so, it was necessary to create a Figure of Merit (FoM) which was specific to each tracklet and measured its quality. In all the cases in which

a least-squares procedure has been performed, the FoM used was

$$FoM = -\frac{1}{\det(\boldsymbol{C})} \tag{23}$$

where $\boldsymbol{C}$ is the covariance matrix in Cartesian state obtained after the last refinement possible. This parameter was naturally chosen to indicate the precision of the refined state vector. This aspect also takes into account that a combined refinement, through optical and radar measurements, returns a better covariance matrix (whose eigenvalues are smaller) and consequently a larger negative FoM, which is consistent with a minimization problem. In Fig. 4, we have summarized the algorithm for both strategies.

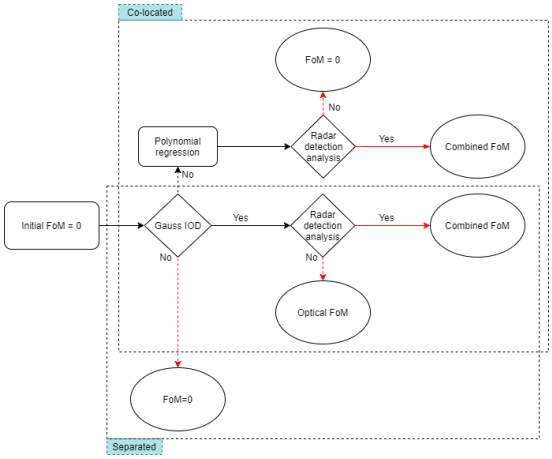

Figure 4. FoM assignment to one tracklet for optical FoV Optimization

For each tracklet we assigned an initial FoM equal to zero. While with the separate strategy the tracklet cannot be used in any meaningful way (and thus its FoM remains null) if Gauss convergence fails, in the co-located strategy we can try, through polynomial regression, to detect the object on the radar and to obtain an IOD which will be refined according to the procedure discussed in 4.3. In both cases, if Gauss convergence succeeds we have at least a covariance matrix from optical least-squares refinement which can be further improved if the radar detection probability, as explained in 4.1, is high. In order to find the optimal solution we have to create an objective function by using FoM introduced before. The objective function we implemented takes an optical camera pointing as input, and returns the score, above mentioned, equal to the sum of the FoMs of the tracklets seen thanks to that pointing.

Fig. 5 shows with a red rectangle the optimized optical FoV, and in black all the tracklets within sight of an observatory. According to [2], the visibility of satellites from a given observatory varies during the year, so the optimization provides one optimized FoV for one observatory during one month. In this case, for the month of July the shown FoV will have a score equal to the sum of the FoM of the tracklets viewed (in black dots). Instrumentation errors and DP make the output of the objective

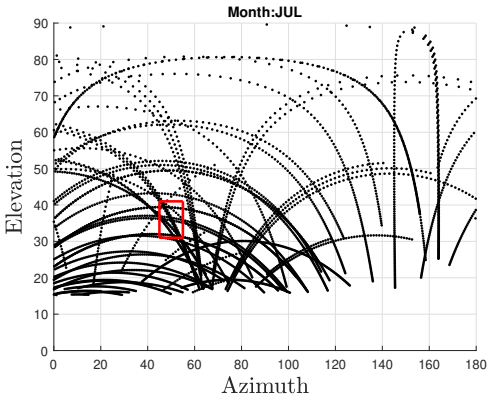

Figure 5. Example of an optimized FoV

function a random variable. It means that different calls of the optimization process do not return the same optical FOV. For this reason, the final optimized optical FoV was obtained by averaging a sufficient number of optimized optical FOV realizations.

5. TEST CASE AND RESULTS

The aim of this section is to show the potential, and eventually the limits, of taking combined measurements and to highlight the related effects on the precision of the associated orbit determination. Here we detail the choice of samples of space objects used to obtain results that are representative for the population of objects we want to focus on. Then, a brief description of the observatories we implemented in the VO and the input data we used for simulation follow. Lastly, we present the overall results obtained for a specific simulated object's trajectory.

5.1. Statistical choice of samples

The detection of unknown objects can force us to make difficult choices in terms of input parameters to carry out reliable simulation studies. As we focus on the detection of LEO objects, a statistical study on the population of known LEO satellites was necessary to collect information on their distribution according to specific orbital parameters of major interest. For this reason, we extracted samples with particular inclination and semi-major axis from approximately 15,000 thousand TLEs of LEO satellites downloaded from *space-track* [13].

We can see clearly that the population of known LEO objects presents some particular features. Concerning the semi-major axis, there are two obvious concentrations which take place between 7200 km and 7850 km. For the inclination, we note that the population concentrates at very narrow inclination ranges; between these ranges the quasi-polar inclinations (from 96° to 103°) present the higher number of LEO satellites. We extracted ten

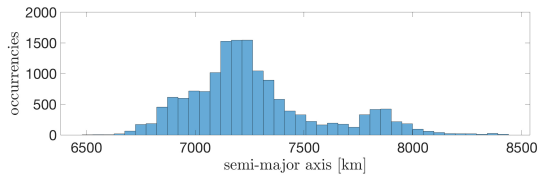

Figure 6. Distribution of known LEO objects according to semi-major axis

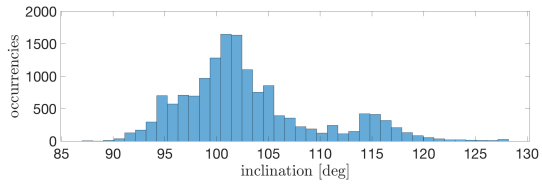

Figure 7. Distribution of known LEO objects according to inclination

LEO satellites according to these distributions in order to simulate possible unknown LEO objects trajectories. Furthermore, in order to take into account the wide variety of sizes of the objects we are interested in, we use a random simulator to fix their Radar Cross Section (RCS). Considering a circular shape, for each passage of the object recorded by the observatory, we selected a different diameter from a uniform distribution within the interval $[0.2, 1.12]$ m. In this way we are able to use the orbital characteristics of only ten samples to simulate a more varied number of space objects in terms of size.

5.2. Observatories description

The location of observatories is of great importance due to its effect on object detectability. As discussed in Section 2, the installation of a radar observatory is very expensive so the best choice for a low-cost system is to use already existing radars and then to position an optical camera in the most convenient place according to one of the strategies detailed above. In particular, we analysed three radar observatories located in France, whose instrumentation present the same characteristics. Concerning the optical camera, we considered four possible placements. One of them corresponds to the separate strategy, and the other three correspond to co-located strategy, which requires the same location for radar and optical observations. In Table 1 we summarize the geographical information about these observatories

Table 1. Observatories

Observatory	Description	Lon [°]	Lat [°]	Alt [km]
SATAM 1	Radar and/or Optical	-0.3	44.2	0.119
SATAM 2	Radar and/or Optical	4.5	49.3	0.137
SATAM 3	Radar and/or Optical	9.4	41.9	0
Pic du Midi	Only Optical	0.14	42.94	2.8

From now on, radar observatories will be referred to as *CoLoc* to emphasize their use for the co-located strategy, while the optical one will be referred to as *Sep*.

5.3. Data for simulations

Table 2. Data set for simulations

Parameter	Symbol	Numerical Value
Radar Field of View	FoV^R	$0.5° \times 0.5°$
Optical Field of View	FoV^O	$10° \times 10°$
Optical Camera RA Standard Deviation	σ_α	10 ”
Optical Camera Dec Standard Deviation	σ_δ	10 ”
Radar Range Standard Deviation	σ_ρ	$25\ m$
Limiting Visual Magnitude	$\bar{V}$	13
Optical Camera Image Rate	Δt_{IR}	$3\ s$
Azimuth slew rate	$\dot{A}_R$	$30\ °/s$
Elevation slew rate	$\dot{h}_R$	$30\ °/s$
t_{IPF} for co-located strategy	t_{IPF}	$20\ s$
t_{IPF} for separate strategy	t_{IPF}	$30\ s$

Here we report in detail all the data we used for simulations carried out with the VO, always referring to Table 2. Further details about the definition of some values needed by the VO can be found in [11]. As we have already stated, each sensor is characterized by its own FoV. The radar's FoV was set to a typical value of sensors used for orbital debris monitoring. For the optical camera, the choice was carefully considered following the exhaustive analysis of different aperture diameters and lens shown in [2]. Finally, considering the context of our research, a large FoV going from $10° \times 10°$ to $15° \times 15°$ was possible, and the first was selected. By using the results found in [10], which also show the link between the FoV's width and the noise, the precision of the observation was modelled as a white noise and thus was considered as a Gaussian random variable with zero mean and σ standard deviation, specifically given by optical or radar sensor. Regarding the constraints for optical sensors measures, we considered the optical signatures of orbital debris. By convention, optical signatures use the visual magnitude system adopted from astronomers. It measures the brightness of an astronomical object observed from the Earth. For the purposes of our research, highlighted in Section 1, we needed to define a limit to visual magnitude. According to the results found in [10] and [2], which investigated the detection capabilities of different large FoV optical sensors, we calculated a proper value for the quantity $\bar{V}$ by considering the altitudes, the optical FoV, and the sizes of interest. So, for an object with an altitude around 800 km, a size around 10 cm and an elevation of the sensor's FoV around 30°, we get a good approximation for this constraint with a value of 13. Concerning the image rate of the optical camera, once all the other parameters were defined, gap times between the image frames were set to 3 s and the exposure time was 0.1 s, where the latter is the length of time when the digital sensor inside the camera is exposed to light. We are thus considering a short exposure time setting for our staring camera, which allows for more images over a certain period of time with respect to the long exposure time setting (for more information on

optical cameras typologies and performances, see [2]). Lastly, the time needed for processing the images taken by the optical camera, and for obtaining the chasing law, was chosen differently for the two strategies. Considering the need for two facilities to communicate, we set the time with a higher value for the second strategy.

5.4. Search for optimal FoV

In this section we present some results of the algorithm described in section 4.4. We would like to point out that a lower limit was set for the elevation in the algorithm in order to take into account the exponential increase in background radiance under $30°$, which undermines the detectability of instrumentation (more details in [10]). Both strategies have many features in common concerning the pointing of Optical FoV. The following tables report optimized FoVs for both strategies, considering TLEs data referring to the first ten days of the months of January, March, July and November. These months were chosen according to [2], because they can be considered representative of the visibility conditions in one entire year. For each month, the first line refers to optimized azimuth intervals, and the second to elevation.

Table 3. Optimized optical FoVs for co-located strategy

		CoLoc 1	CoLoc 2	CoLoc 3
Jan	az	$[358.2°, 8.2°]$	$[352°, 2°]$	$[355.7°, 5.7°]$
	el	$[38.8°, 48.8°]$	$[46.8°, 56.8°]$	$[36.8°, 46.8°]$
Mar	az	$[354°, 4°]$	$[353.5°, 3.5°]$	$[357.3°, 7.3°]$
	el	$[36°, 46°]$	$[44°, 54°]$	$[33.9°, 43.9°]$
Jul	az	$[353.6°, 3.6°]$	$[359°, 9°]$	$[353.7°, 3.7°]$
	el	$[36°, 46°]$	$[40.5°, 50.5°]$	$[38.6°, 48.6°]$
Nov	az	$[356.1°, 6.1°]$	$[356.2°, 6.2°]$	$[355.1°, 5.1°]$
	el	$[36.7°, 46.7°]$	$[41.5°, 51.5°]$	$[33.6°, 43.6°]$

Table 4. Optimized FoVs for separate strategy

		Sep
Jan	az	$[4.2°, 14.2°]$
	el	$[39.4°, 49.4°]$
Mar	az	$[2.8°, 12.8°]$
	el	$[32°, 42°]$
Jul	az	$[348.8°, 358.8°]$
	el	$[35.2°, 45.2°]$
Nov	az	$[6.2°, 16.2°]$
	el	$[32.7°, 42.7°]$

We can notice how, for both strategies, the optimized FoV tends to point at low elevations and at northern azimuths. Low elevations are worse than high ones considering optical visibility constraints, but they also involve longer tracklets that usually provide a better context for performing IOD calculations. Northern azimuths can be explained by the fact that most satellites have a polar inclination. In the next tables, we show quantitatively the performances of the algorithm relative to the simulations over the four months. We compared the optimized FoV (Opt) to the following $[0°, 10°] \times [40°, 50°]$ (NOpt), which would be a typical Optical FoV based on the characteristics of the majority of LEO objects' orbits, as explained earlier in this paragraph. Recalling the random behaviour of measurements acquisition, and consequently of the IODs and radar recaptures, in order to get the most probable values, Tables 5 and 6 report the averages of the analyzed quantities over fifty realizations.

Table 5. Performance comparison between Optimized Optical FoV and Non Optimized Optical FoV: Co-located strategy

	CoLoc 1		CoLoc 2		CoLoc 3	
	Opt	Nopt	Opt	Nopt	Opt	Nopt
Total Number in FoV^O	25	17	22	28	21	21
Total Gauss IOD	11	9	10	11	12	6
Total O&R IOD	4	1	1	3	0	1
Total Radar Recaptures	13	9	10	9	11	7

Table 6. Performance comparison between Optimized Optical FoV and Non Optimized Optical FoV: Separate strategy

	Sep	
	Opt	Nopt
Total Number in FoV^O	18	14
Total Gauss IOD	12	5
Total Radar Recaptures	5	4

Total Number in FoV^O represents all the tracklets seen by the optical camera during these four months, with the exception of the so-called sparse observations [5]. *Total Gauss IOD* represents those tracklets for which an IOD with the Gauss method was accomplished. *Total O&R IOD* represents the number of tracklets for which the Gauss method did not converge, but an IOD with the method described in 4.3 was successful. This is present only in the co-located strategy for evident reasons. Concerning *Total Radar Recaptures*, we have to distinguish between the two strategies. In the co-located strategy, it represents the number of tracklets for which recapture with the co-located radar was possible. In the separate strategy, it represents the number of tracklets for which at least one of the radar observatories was able to recapture the satellite. Concerning the co-located strategy, it should be noted that almost all the parameters increased with the optimized FoV. Above all, the difference in the parameter *Total Radar Recaptures*, which gives the number of the most precise OD, clearly shows the importance of an optimization algorithm. Concerning the separate strategy, we have a satisfying number of Gauss IOD but the num-

ber of radar recaptures is disappointing. This means that the chasing law derived from Gauss IOD, and corrected by a least-squares refinement, is too imprecise to allow the radar instrument to take range measurements. We underline that these results are obtained considering only a population of ten TLEs, so it is easy to understand its potential compared to the real problem of detecting and cataloguing thousands of new space objects. The large number of surveys we would have to deal with in real life, highlights how this tool plays a fundamental role in this problem.

5.5. Detailed results of a co-located case

In this section, we present some representative results of the strategy with co-located observatories. We focus on the differences in OD precision between each step of the cataloguing process of one specific simulated trajectory. The observatory, period of time and Optical FoV which were used for the simulation are summarized in the following table

Table 7. Input for co-located simulation example

Observatory	Period of time	Optical FoV
CoLoc 1	From: 2019 MAR 01 08:56:54	az $[354°, 4°]$
	To: 2019 MAR 09 20:49:56	el $[36°, 46°]$

The choice of this optical FoV derives from the optimization analysis discussed in 4.4. These inputs, together with the data set specified in Table 2, gave interesting results in terms of the number of detected tracklets and the possibility of returning high precision OD.

Table 8. Tracklets Analysis

Number of Tracklets	Number of Tracklets in FoV^O	Number of Gauss' IOD	Number of recaptures
13	3	2	3

The first parameter represents the total number of tracklets that could be visible from the optical observatory, while the second represents the tracklets which actually entered the selected optical FoV. Even if the number of Gauss' IOD is two, the number of recaptures is three, meaning that the radar chased the object correctly twice thanks to Keplerian propagation of only optical least-squares refined IOD, and once thanks to polynomial regression of right ascension and declination. This result is very important because it shows how the method presented in 4.3 gives us the opportunity of obtaining an OD in such cases, usually present in non-negligible number, for which IOD with Gauss's method fails. This aspect also represents a great advantage of the co-located strategy for which O&R IOD is exclusively applied.

In Table 9, we can find a comparison between the Modified Equinoctial Elements (MEE) of the target orbit, the

Table 9. From Gauss' IOD to refined OD

MEE	Target orbit from TLE	Optical Gauss' IOD	Optical least-squares	Combined least-squares
p [km]	7084.655160	6328.844550	7195.890865	7085.949663
f [\]	0.000516	-0.059996	0.013449	0.000729
g [\]	0.000039	0.082285	-0.008418	0.000025
h [\]	-0.300780	-0.300569	-0.302580	-0.300801
k [\]	-0.377314	-0.373137	-0.375883	-0.377293
L $[rad]$	-0.874718	-0.878307	-0.876219	-0.874718

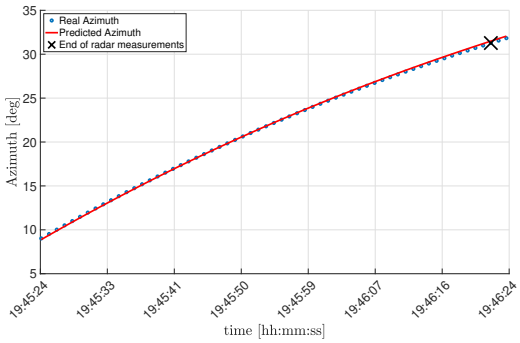

Figure 8. Predicted trajectory through orbit propagation

Gauss IOD, the refined orbit through optical measurements only, and the refined orbit through combined optical and radar measurements. We used MEE because we are dealing with low eccentric orbits, so a representation with typical Keplerian elements could lead to problems in calculating the perigee argument and the true anomaly. It is clear that the Gauss method provides a very imprecise IOD, but we are immediately able to obtain a more accurate orbital knowledge by performing a least-squares refinement with optical measurements. We can then use these results to perform an orbit propagation in Keplerian dynamics and obtain the predicted trajectory of the object both in azimuth and elevation. For simplicity, in Fig. 8 we report only the azimuth chasing law, while underling that, for a successful recapture, both of them have to respect precision constraints over the same period of time. The most interesting result is that, by refining through radar measurements, a very accurate OD is obtained. This highlights once again the importance of combining the two types of measurements because of the high accuracy they can provide for different parameters, i.e. angles from optics and ranges from radar.

We want to compare the accuracy of these results with the OD from O&R IOD case. In Table 10, we present the consecutive refinements of an IOD obtained thanks to a radar chasing law derived from polynomial regression of optical measurements.

In Fig. 9, we note a valid approximation for a very short period of time with respect to the chasing law in Fig. 8; nevertheless it is good enough to allow radar recapture. It is also remarkable how the O&R IOD is quite imprecise, but a combined least-squares refinement considerably reduces the errors returning an OD which is slightly less ac-

Table 10. From O&R IOD to refined OD

MEE	Target orbit from TLE	O&R IOD	Combined least-squares
p [km]	7084.827371	8438.139532	7081.601875
f [\]	0.000431	-0.014261	0.000531
g [\]	-0.000184	-0.216745	0.000387
h [\]	-0.416985	-0.415563	-0.416949
k [\]	-0.243420	-0.247684	-0.243508
L $[rad]$	-1.160880	-1.158311	-1.160785

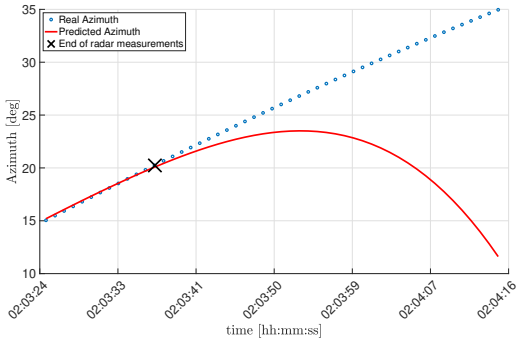

Figure 9. Predicted trajectory through polynomial regression

curate than the previous case; nevertheless, this important result shows how the method developed in 4.3 can compete with a well-affirmed method. In order to compare the precision of the two methods implemented to obtain an IOD, figure 11 compares standard deviations of the MEE after the combined least-squares.

Table 11. MEE Standard deviation comparison between Gauss method and O&R IOD method of final orbits

MEE SD	Gauss IOD Example	O&R IOD Example
σ_p [km]	2.777134	7.928394
σ_f [\]	0.000434	0.004070
σ_g [\]	0.000256	0.002625
σ_h [\]	0.000105	0.001080
σ_k [\]	0.000118	0.002406
σ_L $[rad]$	0.000139	0.002044

In the case of O&R IOD, we usually obtain worse standard deviations, which justifies its application only after Gauss IOD failed, but it remains a useful method for increasing the number of ODs. In both presented cases, sometimes the errors in the parameters can be non-negligible, and nothing prohibits using these rougher ODs for a possible recapture with a higher-cost system in order to further increase their precision. This particular strategy involves data association, as described in [12].

5.6. Detailed results of a separate case

Here we present the results of the strategy with separate observatories. We also report for this case the specific details of the simulation, recalling that the main data reported in Table 2 were used.

Table 12. Input for separate strategy simulation example

Observatory	Period of time	Optical FoV	
Sep	From: 2019 JUL 01 03:47:03	az	$[348.8°, 358.8°]$
	To: 2019 JUL 09 14:01:01	el	$[35.2°, 45.2°]$

Still using an optical FoV found through the optimization algorithm, we can notice in Table 13 how the number of detected tracklets is quite lower than the total number of objects passing within sight of the observatory. The positive aspect is that, as in this example, the initial orbits determined by the Gauss method are usually precise enough to enable their recapturing by the radar.

Table 13. Tracklets Analysis

Number of Tracklets	Number of Tracklets in FoV^O	Number of Gauss' IOD	Number of recaptures
24	4	2	2

Like in the previous section, we can compare the results in terms of MEE by looking at the target orbit. Also, in this case we can see how the IOD is quite imprecise and how the least-squares refinement gives us much better results. We can see in Fig. 10 how the chasing law, always obtained through orbit propagation in Keplerian dynamics, is very precise and allows us to take radar measurements (the chasing law is here reported only in azimuth).

Table 14. From Gauss' IOD to OD separate strategy

MEE	Target orbit from TLE	Optical Gauss' IOD	Optical least-squares	Combined least-squares
p [km]	7084.199021	8422.807782	7173.747674	7075.876869
f [\]	0.000149	0.123371	0.007403	-0.000933
g [\]	-0.000246	-0.131621	-0.009567	0.000423
h [\]	-0.418323	-0.424766	-0.418487	-0.418279
k [\]	-0.241123	-0.239449	-0.241558	-0.241165
L $[rad]$	-0.933082	-0.948536	-0.933905	-0.932976

We can therefore remark the possibility of making combined use of the instruments located in two different observatories thanks to the precise IOD we achieved with this strategy, but we have to consider that further recaptures are needed to make this strategy more advantageous. For the sake of comprehensiveness, we report standard deviations of the MEE of the final orbit in Table 15.

6. CONCLUSION AND FUTURE WORK

This paper presented a novel method for extracting orbital knowledge of a space object by exploiting the com-

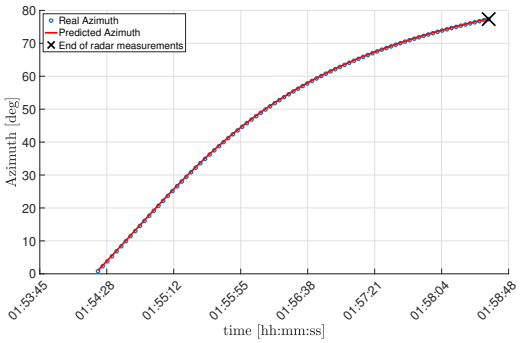

Figure 10. Predicted trajectory through orbit propagation

Table 15. MEE Standard deviation of the final orbit

MEE SD	After combined LS
σ_p [km]	7.778675
σ_f [\]	0.000881
σ_g [\]	0.000693
σ_h [\]	0.000089
σ_k [\]	0.000104
σ_L $[rad]$	0.000134

bined use of optical and radar measurements. Two possible strategies, with co-located or with separate observatories, were investigated to understand their ability to adapt to different needs. They showed they could achieve good results by using any existing radar observatory and low cost optical cameras. The optimization algorithm to find the optimal optical FoV for the staring camera, and the method to get an IOD from combined measurements were widely validated. They were of crucial importance to increase system detectability and overcome the problems associated with the convergence of the Gauss method. In fact, the results show that optimal pointing respects the condition of pointing north, because most of LEO satellites are in polar orbits, and at lower elevations to increase visibility and the amount of objects seen. We can also mention how the uncertainties related to the OD show the accuracy of the final results. Regarding future work, the increase in the number of samples analysed is certainly one of the most interesting and effective steps in validating all the results obtained. Increasing the number of observatories and differentiating their location can also be a key step in creating a more efficient network of detection systems.

A more accurate and detailed study of input parameters could also give more realistic simulations; above all, the addition of weather constraints could make the separate strategy appear more advantageous than presented in our study, due to the better positioning of the optical instrument. As a last remark, we want to highlight the possibility of using different FoVs for both instruments. A radar's FoV of $1^\circ \times 1^\circ$ could lead to better results for both strategies, and especially for the second one, but this is not the most important parameter to change. For the separate strategy we have to underline the possibility of having an optical instrument in a very favorable position. At these altitudes the noise and the disturbances coming from external factors like the weather or background luminosity, have reduced effects. For this reason, the possibility of using a larger optical's FoV of $15^\circ \times 15^\circ$ could be investigated. This could lead to longer tracklets and thus to a higher probability of having a successful IOD through the Gauss method. A larger FoV would lead to an increase in the measurement noise because of the larger aperture diameter and pixel size, but this would be compensated by the increase in visibility mentioned before, leading to an acceptable overall situation in terms of disturbances.

REFERENCES

1. T. Yanagisawa, H. Kurosaki, H. Oda, M. Tagawa. *Ground-based optical observation system for LEO objects (2015).*
2. Thomas Hasenohr. Master's thesis. *Initial Detection and Tracking of Objects in Low Earth Orbit.*
3. Michael A. Steindorfer, Georg Kirchner, Franz Koidl, Peiyuan Wang, Alfredo Anto, Jaime Fernàndez Sànchez, Klaus Merz. *Stare and chase of space debris targets using real-time derived pointing data (2017).*
4. *NAIF, Navigation and Ancillary Information Facility* `https://naif.jpl.nasa.gov/naif/`
5. Laura Pirovano. PhD thesis. *Cataloguing space debris: Methods for optical data association (2019).*
6. Howard D. Curtis. *Orbital Mechanics for Engineering Students, Third edition (2014).*
7. David A.Vallado. *Fundamentals of Astrodynamics and Applications, Fourth edition (2013).*
8. K. W. Vugrin, L. P. Swiler, R. M. Roberts, N. J. Stucky-Mack, S. P. Sullivan. *Confidence region estimation techniques for nonlinear regression in groundwater flow (2007).*
9. Michal J. Dichter, Jeremy J. Wojcik. *Characterizing the Convergence Behavior of Gauss's Method of Initial Orbit Determination (2020).*
10. James R. Shell. *Optimizing orbital debris monitoring with optical telescopes.*
11. M. Rasotto, G. Di Mauro, R. Laugier *Technology for Improving Re-Entry Predictions of European Upper Stages through Dedicated Observations.*
12. A.Vananti, T. Schildknecht, J. Siminski, B. Jilete, T. Flohrer. *Tracklet-Tracklet correlation method for radar and angle observations.*
13. *Space Track* `https://www.space-track.org/`